Interferometric imaging condition for wave-equation migration

Paul Sava* and Oleg Poliannikov†

* *Center for Wave Phenomena, Colorado School of Mines, Golden CO 80401, USA*
† *Department of Mathematical Sciences, Colorado University, Denver, CO 80217, USA*

ABSTRACT

The fidelity of depth seismic imaging depends on the accuracy of the velocity models used for wavefield reconstruction. Models can be decomposed in two components corresponding to large scale and small scale variations. In practice, the large scale velocity model component can be estimated with high accuracy using repeated migration/tomography cycles, but the small scale component cannot. Therefore, wavefield reconstruction does not completely describe the recorded data and migrated images are perturbed by artifacts.

There are two possible ways to address this problem: improve wavefield reconstruction by estimating more accurate velocity models and image using conventional techniques (e.g. wavefield cross-correlation), or reconstruct wavefields with conventional methods using the known smooth velocity model, and improve the imaging condition to alleviate the artifacts caused by the imprecise reconstruction, as suggested in this paper.

In this paper, the unknown component of the velocity model is described as a random function with local spatial correlations. Imaging data perturbed by such random variations is characterized by statistical instability, i.e. various wavefield components image at wrong locations that depend on the actual realization of the random model. Statistical stability can be achieved by local wavefield averaging either in spatial windows defined in the vicinity of the data acquisition locations, or in local windows defined in the vicinity of image points. We use the latter approach and show that the technique is effective in attenuating imaging artifacts without being hampered by some of the limitations of data-space alternatives.

Key words: imaging, interferometry, random media

1 INTRODUCTION

Seismic imaging in complex media requires accurate knowledge of the medium velocity. Assuming single scattering, imaging requires propagation of the recorded wavefields from the acquisition surface, followed by the application of an imaging condition highlighting locations where scattering occurs, i.e. where reflectors are present.

The main requirement for good-quality imaging is accurate knowledge of the velocity model. Errors in the model used for imaging lead to inaccurate reconstruction of the seismic wavefields and to distortions of the migrated images. In a realistic seismic experiment the velocity model is not known exactly. Migration velocity analysis produces large scale approximations of the model, but fine scale variations remain elusive. For example, when geology includes complicated stratigraphic structures, the rapid velocity variations on the scale of the seismic wavelength and smaller cannot be estimated correctly. Therefore, even if the broad kinematics of the seismic wavefields are reconstructed correctly, the extrapolated wavefields also contain distortions that lead to image artifacts obstructing the image of the geologic structure under consideration. While it is certainly true that even the recovery of a long-wave background may prove to be a challenge in some circumstances, we do not attempt to address that issue in this paper. Instead, we concentrate solely on the problem of dealing with the effect of a small scale random variations.

There are two ways in which we can approach this problem:

- The first option is to improve the velocity analysis methods to estimate the small-scale variations in the model. Such techniques take advantage of all information contained in seismic wavefields and are not limited to kinematic information of

selected events picked from the data. Examples of techniques in this category are waveform inversion (Tarantola, 1987; Pratt and Worthington, 1990; Pratt, 1990), wave-equation tomography (Woodward, 1992) or wave-equation migration velocity analysis (Sava and Biondi, 2004a; Sava and Biondi, 2004b; Shen et al., 2005). A more accurate velocity model allows for more accurate wavefield reconstruction. Then, wavefields can be used for imaging using conventional procedures, e.g. cross-correlation.

- The second option is to concentrate on the imaging condition, rather than concentrate on wavefield reconstruction. Assuming that the large-scale component of the velocity models is known (e.g. by iterative migration/tomography cycles), we can design imaging conditions that are not sensitive to small inaccuracies of the reconstructed wavefields. Imaging artifacts can be reduced at the imaging condition step, despite the fact that the wavefields incorporate small kinematic errors due to velocity fluctuations.

The two options are complementary to each other, and both can contribute to imaging accuracy. In this paper, we concentrate on the second approach. For purposes of theoretical analysis, it is convenient to model the small-scale variations velocity fluctuations as random but correlated variations superimposed on a smooth known velocity. We assume that we know the smooth background, but we do not know the random fluctuations. The goal is to design an imaging condition that alleviates artifacts caused by those random fluctuations.

Conventional imaging consists of cross-correlations of extrapolated source and receiver wavefields at image locations. Since wavefield extrapolation is performed using an approximation of the true model, the wavefields contain random time delays, or equivalently random phases, which lead to imaging artifacts.

One way of mitigating the effects of the random model on the quality of the resulting image involves using techniques based on acoustic time reversal (Fink, 1999). A well-known result is that, under certain assumptions, a signal sent through a random medium, recorded by a receiver array, time reversed and sent back through the same medium, refocuses at the source location in a statistically stable fashion. Statistical stability means that the refocusing properties (i.e. image quality) are independent of the actual realization of the random medium (Papanicolaou et al., 2004; Fouque et al., 2005).

An equivalent formulation of this result is that statistical stability can be achieved if random phase shifts between signals recorded at nearby locations are removed by cross-correlation, prior to back propagation into the medium. This observation lies at the heart of coherent interferometric imaging (Borcea et al., 2005; Borcea et al., 2006c; Borcea et al., 2006a; Borcea et al., 2006b) or imaging and velocity analysis in presence of uncertain models (Dussaud, 2005). With this approach, local spatial cross-correlations of data traces on the acquisition surface are computed and extrapolated to the image location using standard techniques. Thus, random phase shifts that cause imaging artifacts are removed prior to extrapolation and imaging quality in the smooth background medium increases. This method assumes the existence of a continuous acquisition array with dense receiver layout to ensure coherency of local cross-correlations.

We investigate an alternative way of using time reversal to increase imaging statistical stability. Instead of coherent interferometry applied to data on the acquisition surface, we first extrapolate wavefields to all locations in the imaging volume and then apply local spatial cross-correlations in the vicinity of every image point. Correlations in the image-space damps small random fluctuations in the extrapolated wavefields. The cross-correlations do not relocate energy in space, but simply produce local averages of the extrapolated wavefields.

The procedure closely resemble conventional imaging procedures where wavefields are extrapolated in the image volume and then cross-correlated in time at every image location. Our method uses averaging in three-dimensional local windows around image locations. From implementation and computational cost points of view, our technique does not differ much from conventional imaging, although the imaging properties are improved. Therefore, we use the name *interferometric imaging condition* for our technique to contrast it with conventional imaging condition which represents a special case of this method for infinitely small local windows.

One advantage of using the interferometric imaging condition in wave-equation migration is that it also makes efficient use of the data obtained by a sparse array, since the cross-correlation is performed at an image point on wavefields extrapolated from all data traces simultaneously. Furthermore, local averaging around the image locations is inherently three-dimensional, in contrast with the two-dimensional averaging typical for interferometric imaging parametrized on the surface. This increases signal-to-noise ratio and improves random phase cancellation, although it also increases computational cost proportionally. Processing with image-space coordinates is simpler than processing using data-space coordinates because, after extrapolation, wavefields are simpler since wave propagation complications have been unraveled in the extrapolation process (Stolk and Symes, 2004).

Finally, we note that the proposed method is not an extension, but an alternative to coherent interferometry. When assumptions permit, the two methods can be used simultaneously in an imaging functional, thus taking advantage of the best qualities of both approaches.

2 SEISMIC IMAGING CONDITIONS

Conventional seismic imaging methods share the fundamental assumption of single scattering in the subsurface (Born approximation). Under this assumption, we can represent waves recorded at the surface as a convolution of Green's functions (G) corresponding to sources on the surface and scattering points in the subsurface. Assuming an impulsive source, we can write

$$P(\mathbf{x}_m,\omega_m) = G(\mathbf{x}_s,\mathbf{y}_m,\omega_m)\,G(\mathbf{y}_m,\mathbf{x}_m,\omega_m)\ , \qquad (1)$$

where P denotes recorded acoustic data at coordinates $\mathbf{x}_m$, $\mathbf{x}_s$ are coordinates of the source, $\mathbf{y}_m$ are coordinates of the scattering points, and ω_m is the frequency of the propagating wave.

Relation (1) can be written in an equivalent form using time instead of frequency variables, but for simplicity we use the frequency-domain notation throughout this paper. The Green's function G characterizes data propagation in the real medium of velocity v.

Imaging with recorded data $P(\mathbf{x}_m, \omega_m)$ is a two-step procedure:

- The first step consists of extrapolation of source and receiver wavefields from the recording surface to image locations. The source wavefield corresponds to simulated waves propagating forward in time from the source location $\mathbf{x}_s$, and the receiver wavefield corresponds to waves propagating backward in time from recording locations $\mathbf{x}_m$.
- The second step consists of an imaging condition evaluating whether the two extrapolated wavefields match kinematically, which indicates whether a reflector is present in the medium.

Wavefield extrapolation and imaging can be implemented in different space and time domains, for example downward continuation with the one-way wave-equation implemented in frequency-wavenumber, frequency-space or mixed domains, or wavefield extrapolation with the two-way wave-equation in time-space, etc. Wavefield extrapolation can also be performed using Kirchhoff integral methods followed by conventional imaging. However, the actual extrapolation method is irrelevant for the discussion in this paper. For simplicity, we represent wavefield extrapolation with Green's functions in the frequency-domain, although our examples use time-domain two-way finite-difference solutions to the acoustic wave-equation, process typically known as reverse-time migration (Kosloff and Baysal, 1983). Any other implementation of Green's functions can be substituted in our discussion with no change to the conclusions.

In real imaging projects, the actual velocity medium is not known in detail, therefore the known velocity model represents a smooth version of the real model. This smooth model does not incorporate rapid variations of the velocity at scales comparable with or smaller than the seismic wavelength. In this paper, we represent the real model with random variations by symbol $v(x,y,z)$, and the approximate (possibly smooth) model by symbol $v_0(x,y,z)$.

When reconstructing wavefields in seismic imaging, we compute Green's functions connecting points on the acquisition surface with image points in the subsurface. We use the symbol G_0 to denote Green's functions computed in the approximate medium of velocity v_0, in contrast with the symbol G which denotes Green's functions representing wave propagation in the real medium of velocity v.

Using these notations and assuming an impulsive source function, the source wavefield reconstructed during imaging by propagation forward in time from the source position is represented as $G_0(\mathbf{x}_s, \mathbf{y}_m, \omega_m)$, and the receiver wavefield reconstructed by propagation backward in time from the receiver positions is represented as $P(\mathbf{x}_m, \omega_m)\overline{G_0(\mathbf{y}_m, \mathbf{x}_m, \omega_m)}$, where the over-line represents complex conjugation for propagation backward in time.

2.1 Conventional imaging condition

The conventional way of implementing the imaging condition for wave-equation migration involves cross-correlation of the source and receiver wavefields, often referred to as the $U\overline{D}$ imaging condition (Claerbout, 1985), where D and U stand for downward and upward propagating wavefields. The image I is evaluated using the relation

$$I(\mathbf{y}_m) = \int_{\omega_m} d\omega_m \int_{\mathbf{x}_m} d\mathbf{x}_m \; \overline{G_0(\mathbf{x}_s, \mathbf{y}_m, \omega_m)} P(\mathbf{x}_m, \omega_m) \overline{G_0(\mathbf{y}_m, \mathbf{x}_m, \omega_m)} \; . \qquad (2)$$

This imaging condition evaluates the match between source and receiver wavefields reconstructed throughout the medium. Maximum energy at zero temporal cross-correlation lag, computed by summation over temporal frequency, indicates the presence of reflectors. Here and for the rest of the paper, summation over multiple seismic experiments (sources) is assumed.

The propagation geometry of the imaging condition (2) is summarized in figure 1(a): source waves are propagated forward in time from the source at $\mathbf{x}_s$ to the scatterer location $\mathbf{y}_m$, and receiver waves are propagated backward in time from the receiver coordinates $\mathbf{x}_m$ to the scatterer location $\mathbf{y}_m$.

The assumption made in this model is that the Green's functions used for reconstruction are accurate representations of the Green's functions describing wave propagation in the real medium. However, for the case of media with random velocity fluctuations, v_0 is a smooth velocity approximating v. Thus, although the general kinematics of wave propagation are accurately described by v_0, the velocity fluctuations induce perturbations of the wavefield leading to imaging artifacts.

For illustration of those imaging artifacts, consider the numerical modeling in figures 3(a)-3(f). Figures 3(a)-3(e), depict in the background the velocity smooth model v_0, and figures 3(b)-3(f) depict in the background the velocity real model v. Overlayed are the seismic wavefields for a point source on the surface at $x = 600$ m which generates secondary waves from 3 scatterers represented in the figures around $x = 600$ m and $z = 700$ m. Panels (b) and (d) simulate Green's functions in the real model with random fluctuations, and panels (a) and (c) simulate the reconstructed Green's functions in the smooth model. Top row panels correspond to an early time prior to the source wavefield interacting with the scatterers, and the bottom row corresponds to a later time and depicts scattered wavefields from the imaging targets. Figures 4(a)-4(b) show the recorded data on the acquisition surface. For the case of media with random fluctuations, we observe that the wavefronts for the scattered wavefields resemble the corresponding wavefronts in the smooth media. Since we are imaging with the smooth velocity, these wavefronts are the only contributions of the recorded data to the image. The random fluctuations (time delays) incorporated in those wavefields are not compensated in the imaging process and lead to artifacts.

The main question we address here is: what is the impact of migrating data simulated in the random model depicted in figures 3(b)-3(f) with the smooth model depicted in figures 3(a)-3(e)?

- Figure 5(a) shows the result of migrating with smooth velocity v_0 data simulated with the same velocity v_0. Panel 5(c) depicts a zoom on the image in figure 5(a). The images show well-focused diffractors and typical truncation artifacts produced by the limited acquisition on the surface.
- Figure 5(b) shows the result of migrating with smooth velocity v_0 data simulated with the random velocity v. Panel 5(d) depicts a zoom on the image in figure 5(b). The images show the 3 diffractors and the truncation artifacts, together with many other artifacts caused by imaging with an incorrect velocity v_0.

Suppressing artifacts exemplified by figures 5(b) and 5(d) is the focus of this paper. If imaging targets correspond to stratigraphy characterized by finely-spaced reflectors, the artifacts caused by random velocity variation can obscure valuable information and hinder geologic interpretation.

2.2 Coherent interferometry

One way of addressing the problem of imaging in models with random fluctuations involves statistical stabilization using phase compensation in windows localized in time and space (Papanicolaou et al., 2004; Fouque et al., 2005). The idea is that small wavefield fluctuations caused by random perturbations of the velocity model are incoherent spatially and temporally and cancel-out by local cross-correlation and averaging.

The idea of statistical stability for imaging in random media is exploited by the technique called *coherent interferometric imaging* (Borcea et al., 2006b). The main idea of this method is to reduce the delay spread caused by the random fluctuations of the medium using averages of local cross-correlations between nearby traces on the acquisition surface. It has been shown that interferometric imaging methods are capable of reducing imaging artifacts and statistically stabilizing the image by averaging locally in space and time (or frequency) the fluctuations caused by the random variations of the medium.

When constructing an imaging functional, the emulated source wavefield reconstructed with the help of the smooth velocity v_0 contains no random fluctuations, and thus requires no stabilization. All random fluctuations are contained through the recorded data to the receiver wavefield. The latter then requires averaging using interferograms localized in space and time, but the former does not. The modified imaging functional takes the form

$$\begin{aligned} I(\mathbf{y}_m) \quad = \quad & \int\limits_{\omega_m} d\omega_m \int\limits_{|\omega_h|\le\Omega/2} d\omega_h \int\limits_{\mathbf{x}_m} d\mathbf{x}_m \int\limits_{|\mathbf{x}_h|\le X/2} d\mathbf{x}_h \\ & \overline{G_0\left(\mathbf{x}_s,\mathbf{y}_m,\omega_m-\omega_h\right)\Big(P\left(\mathbf{x}_m-\mathbf{x}_h,\omega_m-\omega_h\right)\overline{G_0\left(\mathbf{y}_m,\mathbf{x}_m-\mathbf{x}_h,\omega_m-\omega_h\right)}\Big)} \\ & \overline{G_0\left(\mathbf{x}_s,\mathbf{y}_m,\omega_m+\omega_h\right)\Big(P\left(\mathbf{x}_m+\mathbf{x}_h,\omega_m+\omega_h\right)\overline{G_0\left(\mathbf{y}_m,\mathbf{x}_m+\mathbf{x}_h,\omega_m+\omega_h\right)}\Big)}\,, \end{aligned} \tag{3}$$

where $\mathbf{x}_h$ represents a 2D summation variable on the acquisition surface. For seismic experiments without an active source (exploding reflector experiments), the equivalent imaging functional is

$$\begin{aligned} I(\mathbf{y}_m) \quad = \quad & \int\limits_{\omega_m} d\omega_m \int\limits_{|\omega_h|\le\Omega/2} d\omega_h \int\limits_{\mathbf{x}_m} d\mathbf{x}_m \int\limits_{|\mathbf{x}_h|\le X/2} d\mathbf{x}_h \\ & P\left(\mathbf{x}_m-\mathbf{x}_h,\omega_m-\omega_h\right)\overline{G_0\left(\mathbf{x}_m-\mathbf{x}_h,\mathbf{y}_m,\omega_m-\omega_h\right)} \\ & \overline{P\left(\mathbf{x}_m+\mathbf{x}_h,\omega_m+\omega_h\right)\overline{G_0\left(\mathbf{x}_m+\mathbf{x}_h,\mathbf{y}_m,\omega_m+\omega_h\right)}}\,. \end{aligned} \tag{4}$$

The relation $P\left(\mathbf{x}_m-\mathbf{x}_h,\omega_m-\omega_h\right)\overline{G_0\left(\mathbf{y}_m,\mathbf{x}_m-\mathbf{x}_h,\omega_m-\omega_h\right)}$ represents data at position $\mathbf{x}_m-\mathbf{x}_h$ relocated to the image location $\mathbf{y}_m$, and the relation $P\left(\mathbf{x}_m+\mathbf{x}_h,\omega_m+\omega_h\right)\overline{G_0\left(\mathbf{y}_m,\mathbf{x}_m+\mathbf{x}_h,\omega_m+\omega_h\right)}$ represents data at position $\mathbf{x}_m+\mathbf{x}_h$ relocated to the image location $\mathbf{y}_m$ using Green's functions computed in the smooth medium. Cross-correlation occurs at image location $\mathbf{y}_m$ and the propagation geometry from the acquisition surface is schematically depicted in figure 1(b). An image is formed by summation of all interferograms computed around image points from data located on the surface within the decoherence length X. We do not need to worry in this implementation about loss of depth (range) resolution since the statistical stability is achieved by cross-correlation and averaging at the image locations from data reconstructed from all points on the acquisition surface.

2.3 Interferometric imaging condition (IIC)

We can also approach the coherent imaging problem in an alternative way: rather than correlating data on the acquisition surface, we can reconstruct wavefields at all locations in the imaging volume from all locations on the acquisition surface and suppress the random fluctuations in the wavefield by local cross-correlations in small windows around the image point.

Image-space processing as an alternative to data-space processing has been employed in other seismic data processing contexts, for example for imaging passive seismic data (Artman, 2006) or for predicting multiple after wavefield extrapolation (Artman et al., 2007). Here we use a similar idea to attenuating artifacts caused by inaccurate knowledge of velocity during wavefield extrapolation.

For coherent imaging after extrapolation, we can define another decoherence length around an image point Y, which is analogous to the decoherence length defined on the acquisition surface X. The imaging functional corresponding to this case can be written analogously to the one in equation (3) as

$$\begin{aligned} I(\mathbf{y}_m) \quad = \quad & \int\limits_{\omega_m} d\omega_m \int\limits_{|\omega_h|\le\Omega/2} d\omega_h \int\limits_{|\mathbf{y}_h|\le Y/2} d\mathbf{y}_h \\ & \overline{G_0(\mathbf{x}_s, \mathbf{y}_m - \mathbf{y}_h, \omega_m - \omega_h)} \int\limits_{\mathbf{x}_m} d\mathbf{x}_m \, P(\mathbf{x}_m, \omega_m - \omega_h) \, \overline{G_0(\mathbf{x}_m, \mathbf{y}_m - \mathbf{y}_h, \omega_m - \omega_h)} \\ & \overline{\overline{G_0(\mathbf{x}_s, \mathbf{y}_m + \mathbf{y}_h, \omega_m + \omega_h)} \int\limits_{\mathbf{x}_m} d\mathbf{x}_m \, P(\mathbf{x}_m, \omega_m + \omega_h) \, \overline{G_0(\mathbf{x}_m, \mathbf{y}_m + \mathbf{y}_h, \omega_m + \omega_h)}} \,, \end{aligned} \tag{5}$$

where $\mathbf{y}_h$ represents a 3D summation variable around the image point. For seismic experiments without an active source (exploding reflector experiment), the equivalent imaging functional is

$$\begin{aligned} I(\mathbf{y}_m) \quad = \quad & \int\limits_{\omega_m} d\omega_m \int\limits_{|\omega_h|\le\Omega/2} d\omega_h \int\limits_{|\mathbf{y}_h|\le Y/2} d\mathbf{y}_h \\ & \int\limits_{\mathbf{x}_m} d\mathbf{x}_m \, P(\mathbf{x}_m, \omega_m - \omega_h) \, \overline{G_0(\mathbf{x}_m, \mathbf{y}_m - \mathbf{y}_h, \omega_m - \omega_h)} \\ & \overline{\int\limits_{\mathbf{x}_m} d\mathbf{x}_m \, P(\mathbf{x}_m, \omega_m + \omega_h) \, \overline{G_0(\mathbf{x}_m, \mathbf{y}_m + \mathbf{y}_h, \omega_m + \omega_h)}} \,. \end{aligned} \tag{6}$$

The relation $P(\mathbf{x}_m, \omega_m - \omega_h) \, \overline{G_0(\mathbf{y}_m - \mathbf{y}_h, \mathbf{x}_m, \omega_m - \omega_h)}$ represents data at position $\mathbf{x}_m$ relocated to the image location $\mathbf{y}_m - \mathbf{y}_h$, and the relation $P(\mathbf{x}_m, \omega_m + \omega_h) \, \overline{G_0(\mathbf{y}_m + \mathbf{y}_h, \mathbf{x}_m, \omega_m + \omega_h)}$ represents data at position $\mathbf{x}_m$ relocated to the image location $\mathbf{y}_m + \mathbf{y}_h$. Cross-correlation occurs around image location $\mathbf{y}_m$ and the propagation geometry from the acquisition surface is schematically depicted in figure 1(c).

The imaging procedure described by equation (5) exploits two main ideas:

- The first idea is that of extended imaging conditions (Rickett and Sava, 2002; Sava and Fomel, 2006) where multiple space and time lags of the source-receiver wavefield cross-correlation are evaluated. In particular, $\mathbf{y}_h$ is interpreted as a 3D spatial lag of the cross-correlation between the reconstructed source and receiver wavefields. This lag can be used for decomposition of images function of scattering angles (Sava and Fomel, 2003; Fomel, 2004; Biondi and Symes, 2004; Sava and Fomel, 2005). Here, we use $\mathbf{y}_h$ as a summation variable during averaging around image locations.
- The second idea is that we can achieve statistical stability in random media by space and time averaging of wavefield cross-correlations in local windows (Papanicolaou et al., 2004; Fouque et al., 2005). We exploit this idea similarly to the way it is used by (Borcea et al., 2006b) for coherent interferometric imaging in clutter. The local averaging variable $\mathbf{y}_h$ is similar to the local averaging variable $\mathbf{x}_h$, except that $\mathbf{y}_h$ is defined in the image space, around particular image points. Unlike $\mathbf{x}_h$ which is a 2D quantity defined on the acquisition surface, $\mathbf{y}_h$ is a 3D quantity defined in a volume around the image point location. Unlike $\mathbf{x}_h$ which requires close spacing on the acquisition surface, $\mathbf{y}_h$ is defined around image locations and, assuming media with rapid fluctuations that do not introduce large kinematic differences, does not require special sampling assumptions.

Thus, we can describe the imaging method summarized by equation (5) by the name *interferometric imaging condition*, since it acts similarly to the conventional imaging condition, but with robustness with respect to random fluctuations due to local interferometric averaging in windows around image locations.

Using the interferometric imaging functional defined in equation (5) on the simple example described earlier, we obtain the images depicted in figures 6(b) and 6(d). For comparison, figures 5(b) and 5(d) show the equivalent images obtained using the conventional imaging condition defined in equation (2). The images obtained by interferometric imaging show a reduction of the imaging artifacts surrounding the 3 diffractors despite the fact that imaging was performed using a smooth approximation of the random medium.

Even more generally, we can write the interferometric imaging functional by imposing noise cancellation both on the acquisition surface and around the image points. In this case, imaging is performed using a relation like

$$I(\mathbf{y}_m) \quad = \quad \int\limits_{\omega_m} d\omega_m \int\limits_{|\omega_h|\le\Omega/2} d\omega_h \int\limits_{|\mathbf{y}_h|\le Y/2} d\mathbf{y}_h \int\limits_{|\mathbf{x}_h|\le X/2} d\mathbf{x}_h$$

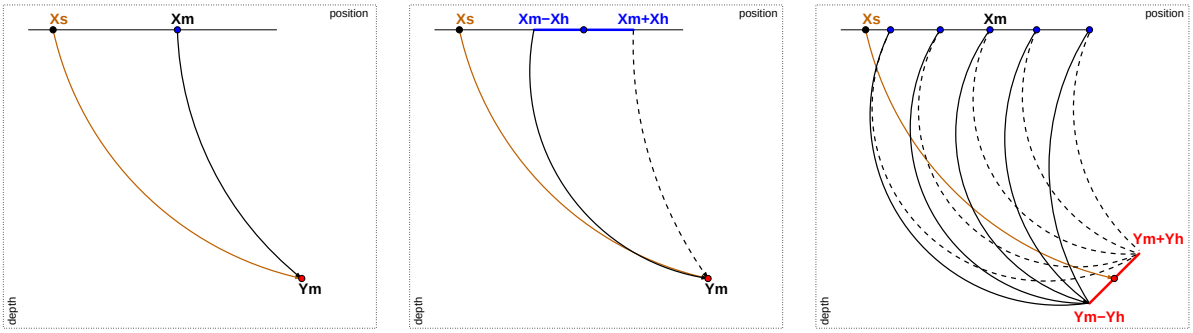


Figure 1. Schematic description of propagation and imaging geometry for various imaging functionals: (a) imaging using equation (2), (b) imaging using equation (3), and (c) imaging using equation (5). Quantity $\mathbf{x}_h$ represents a 1D projection of the 2D averaging variable on the acquisition surface, and quantity $\mathbf{y}_h$ represents a 1D projection of the 3D averaging variable around image points.

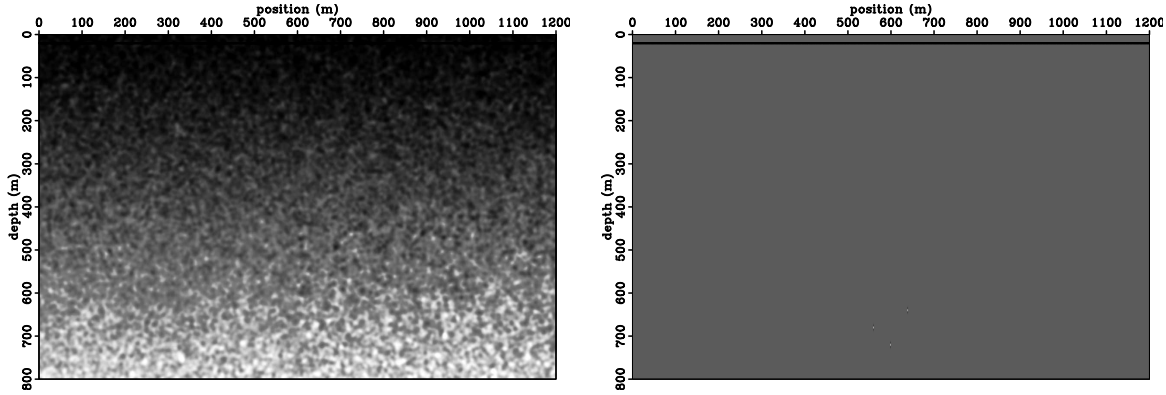


Figure 2. Random velocity model (a) and imaging target located around $x = 600$ m and $z = 700$ m (b).

$$\overline{G_0\left(\mathbf{x}_s,\mathbf{y}_m-\mathbf{y}_h,\omega_m-\omega_h\right)}\int_{\mathbf{x}_m} d\mathbf{x}_m\, P\left(\mathbf{x}_m-\mathbf{x}_h,\omega_m-\omega_h\right)\overline{G_0\left(\mathbf{x}_m-\mathbf{x}_h,\mathbf{y}_m-\mathbf{y}_h,\omega_m-\omega_h\right)}$$
$$\overline{G_0\left(\mathbf{x}_s,\mathbf{y}_m+\mathbf{y}_h,\omega_m+\omega_h\right)}\int_{\mathbf{x}_m} d\mathbf{x}_m\, P\left(\mathbf{x}_m+\mathbf{x}_h,\omega_m+\omega_h\right)\overline{G_0\left(\mathbf{x}_m+\mathbf{x}_h,\mathbf{y}_m+\mathbf{y}_h,\omega_m+\omega_h\right)}\,. \tag{7}$$

For seismic experiments without an active source (exploding reflector experiment), the equivalent imaging functional is

$$\begin{aligned} I(\mathbf{y}_m) \;=\; & \int_{\omega_m} d\omega_m \int_{|\omega_h|\le\Omega/2} d\omega_h \int_{|\mathbf{x}_h|\le X/2} d\mathbf{x}_h \int_{|\mathbf{y}_h|\le Y/2} d\mathbf{y}_h \\ & \int_{\mathbf{x}_m} d\mathbf{x}_m\, P\left(\mathbf{x}_m-\mathbf{x}_h,\omega_m-\omega_h\right)\overline{G_0\left(\mathbf{x}_m-\mathbf{x}_h,\mathbf{y}_m-\mathbf{y}_h,\omega_m-\omega_h\right)} \\ & \overline{\int_{\mathbf{x}_m} d\mathbf{x}_m\, P\left(\mathbf{x}_m+\mathbf{x}_h,\omega_m+\omega_h\right)\overline{G_0\left(\mathbf{x}_m+\mathbf{x}_h,\mathbf{y}_m+\mathbf{y}_h,\omega_m+\omega_h\right)}}\,. \end{aligned} \tag{8}$$

The relation $P\left(\mathbf{x}_m-\mathbf{x}_h,\omega_m-\omega_h\right)\overline{G_0\left(\mathbf{y}_m-\mathbf{y}_h,\mathbf{x}_m-\mathbf{x}_h,\omega_m-\omega_h\right)}$ represents data at position $\mathbf{x}_m-\mathbf{x}_h$ relocated to the image location $\mathbf{y}_m-\mathbf{y}_h$, and the relation $P\left(\mathbf{x}_m+\mathbf{x}_h,\omega_m-\omega_h\right)\overline{G_0\left(\mathbf{y}_m+\mathbf{y}_h,\mathbf{x}_m+\mathbf{x}_h,\omega_m+\omega_h\right)}$ represents data at position $\mathbf{x}_m+\mathbf{x}_h$ relocated to the image location $\mathbf{y}_m+\mathbf{y}_h$.

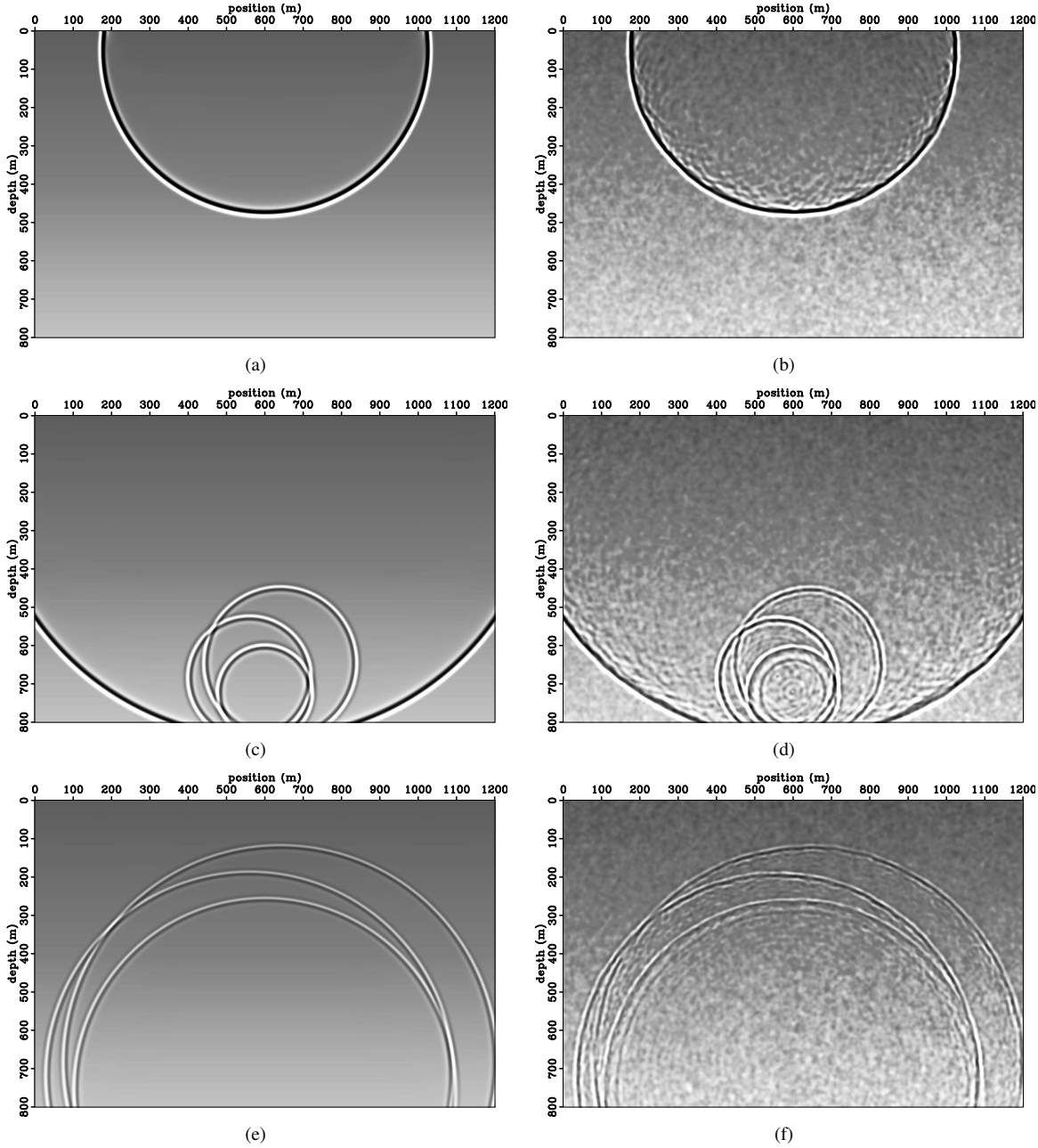


Figure 3. Wavefields simulated in the smooth background velocity v_0, panels (a) and (c) and in the random velocity v, panels (b) and (d).

2.4 Comparison of imaging functionals

At first glance, the imaging functionals (3) and (5) look similar in shape and imaging properties. However, from a practical point of view, the two imaging functionals are fundamentally different:

• Imaging functional (3) achieves statistical stability by cross-correlating and averaging wavefields parametrized function of the location of receivers on the acquisition surface. In this functional, the wavefields subject to cross-correlation are $P(\mathbf{x}_m - \mathbf{x}_h, \omega_m - \omega_h)\overline{G_0(\mathbf{y}_m, \mathbf{x}_m - \mathbf{x}_h, \omega_m - \omega_h)}$ and $P(\mathbf{x}_m + \mathbf{x}_h, \omega_m + \omega_h)\overline{G_0(\mathbf{y}_m, \mathbf{x}_m + \mathbf{x}_h, \omega_m + \omega_h)}$. This operation requires that we reconstruct wavefields at all image locations $\mathbf{y}_m$ for every receiver location on the acquisition surface $\mathbf{x}_m$, for every experiment. This requires to construct solutions of the wave-equation for every trace on the surface acting as an independent source (number of $\mathbf{x}_m$ receivers solutions to the acoustic wave-equation), which is an impractical operation in complex media.

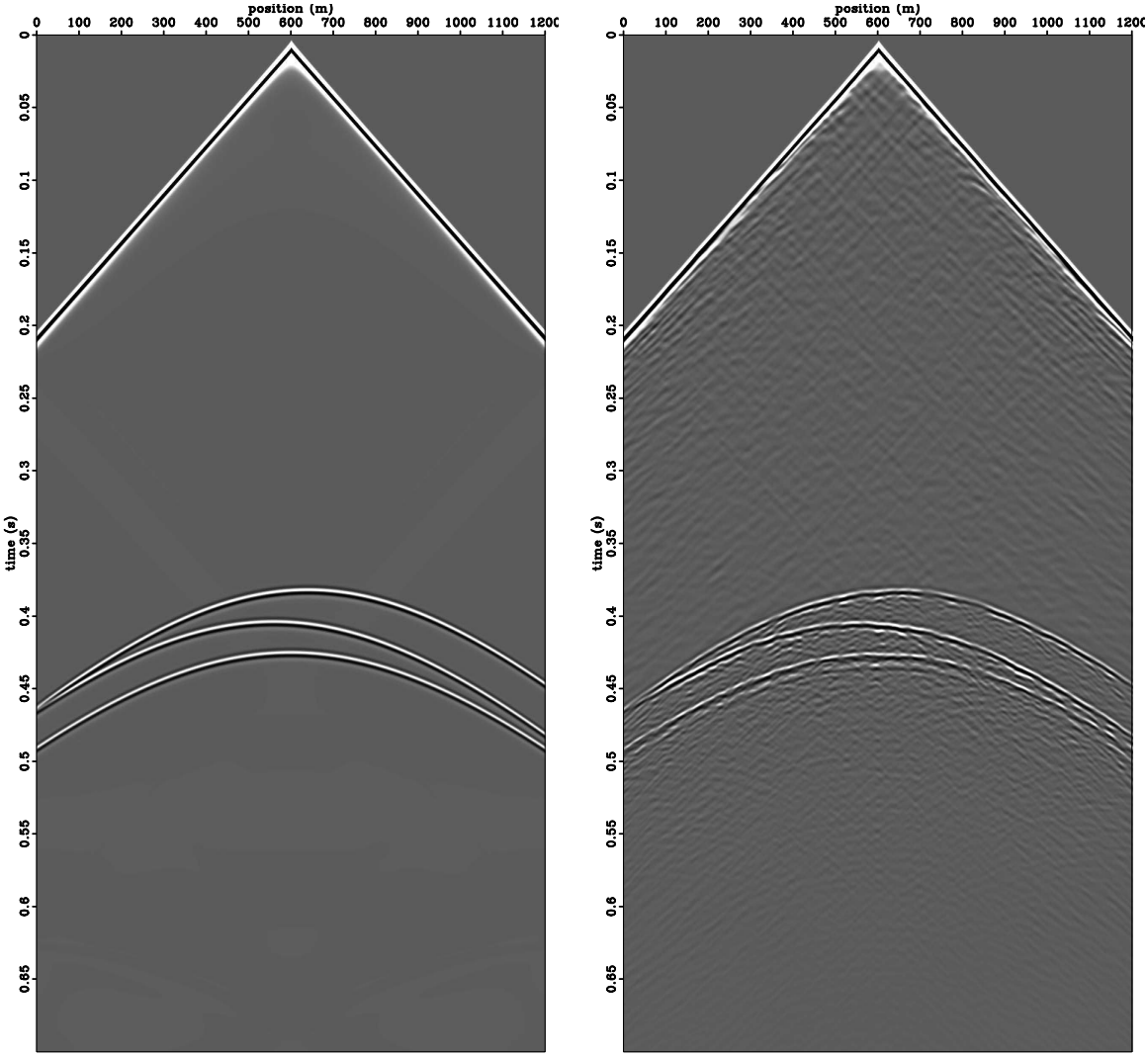


Figure 4. Data recorded for the smooth velocity model, panel (a), and for the model with random velocity variations, panel (b).

• Imaging functional (5) achieves statistical stability by cross-correlating and averaging wavefields parametrized function of the image location. In this functional, the wavefields subject to cross-correlation are $\int\limits_{\mathbf{x}_m} d\mathbf{x}_m\, P(\mathbf{x}_m, \omega_m - \omega_h)\, \overline{G_0(\mathbf{x}_m, \mathbf{y}_m - \mathbf{y}_h, \omega_m - \omega_h)}$ and $\int\limits_{\mathbf{x}_m} d\mathbf{x}_m\, P(\mathbf{x}_m, \omega_m + \omega_h)\, \overline{G_0(\mathbf{x}_m, \mathbf{y}_m + \mathbf{y}_h, \omega_m + \omega_h)}$. This operation requires that we reconstruct wavefields at all image locations $\mathbf{y}_m$ for all receiver locations on the surface $\mathbf{x}_m$, for every experiment. The cost associated with this operation is comparable with the cost of conventional imaging. This requires to construct solutions of the wave-equation for all trace on the surface acting as simultaneous sources (one solution to the acoustic wave-equation), which is an affordable operation in complex media.

3 STATISTICAL STABILITY

The interferometric imaging condition described in the preceding section is used to reduce imaging artifacts by attenuating the incoherent energy corresponding to velocity errors, as illustrated in figures 5(d) and 6(d). The random model used for this example corresponds to the *weak fluctuation regime*, as explained in Appendix A (characteristic wavelength of similar scale with the random fluctuations in the medium and fluctuations with small magnitude).

By statistical instability we mean that images obtained for different realizations of random models with the identical statistics are different. Figures 7(a)-7(d) illustrate data modeled for different realizations of the random model in figures 3(a)-3(f). The general

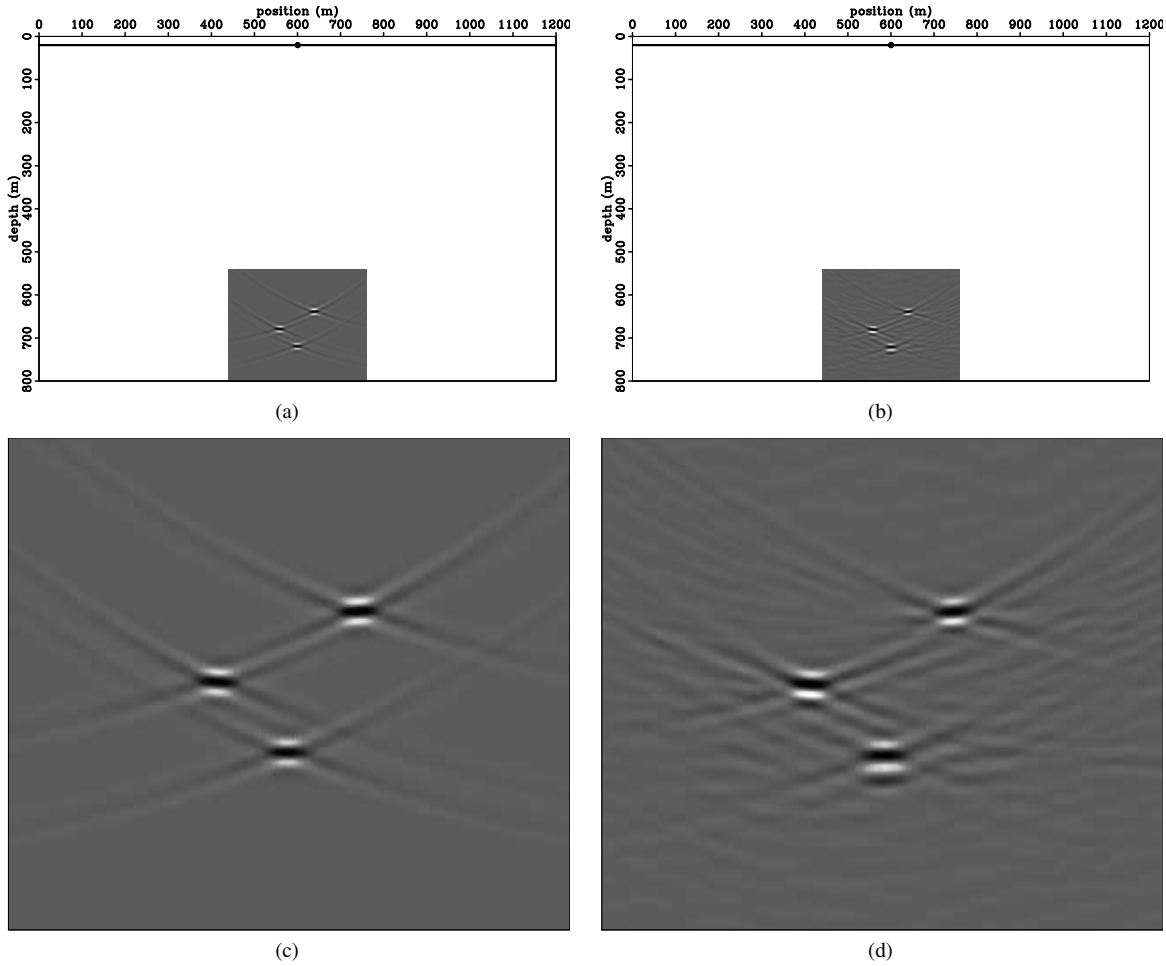


Figure 5. Images produced using the *conventional imaging condition*. Panels (a) and (c) correspond to modeling and imaging in the smooth known velocity model v_0, and panels (b) and (d) correspond to modeling using the random velocity model v and imaging using the smooth velocity model v_0. Panels (c) and (d) depict enlarged versions of the images shown in panels (a) and (b), respectively.

kinematics of the data are the same, but subtle differences exist between the various dataset due to the random model variations. Migration using conventional imaging condition leads to the images in figures 7(e)-7(h) which also show variations from realization to realization. In contrast, figures 7(i)-7(l) show images obtained by the interferometric imaging condition which are more similar to one-another since many of the spurious artifacts have been attenuated.

In typical seismic imaging problems, we cannot ensure that random velocity fluctuations are small (e.g. $\sigma \leq 5\%$). It is desirable that imaging remains statistically stable even in cases when velocity varies with larger magnitude. We investigate the statistical properties of the imaging functional in equation (6) using numeric experiments similar to the one used earlier. We describe the random noise present in the velocity models using the following parameters explained in Appendix A:

- Seismic spatial wavelength $\lambda = 20$ m.
- Wavelet central frequency $\omega = 150$ Hz.
- Background velocity: $v_0 = 3000 + k\,z$ m/s ($k = 1s^{-1}$).
- Random fluctuations parameters: $r_a = 8$, $r_c = 8$, $\alpha = 2$.
- Random noise magnitude σ between 0% and 80%.

This numeric experiment simulates a situation that mixes the theoretical regimes explained in Appendix A: random model fluctuations of comparable scale with the seismic wavelength lead to destruction of the wavefronts, as suggested by the "weak fluctuations" regime; large magnitude of the random noise leads to diffusion of the wavefronts, as suggested by the "diffusion approximation" regime. This combination of parameters could be regarded as a worst-case-scenario from a theoretical standpoint.

Figures 8(a)-8(d) show data sets modeled in models similar to the one in figure 3(b), but where the random noise component

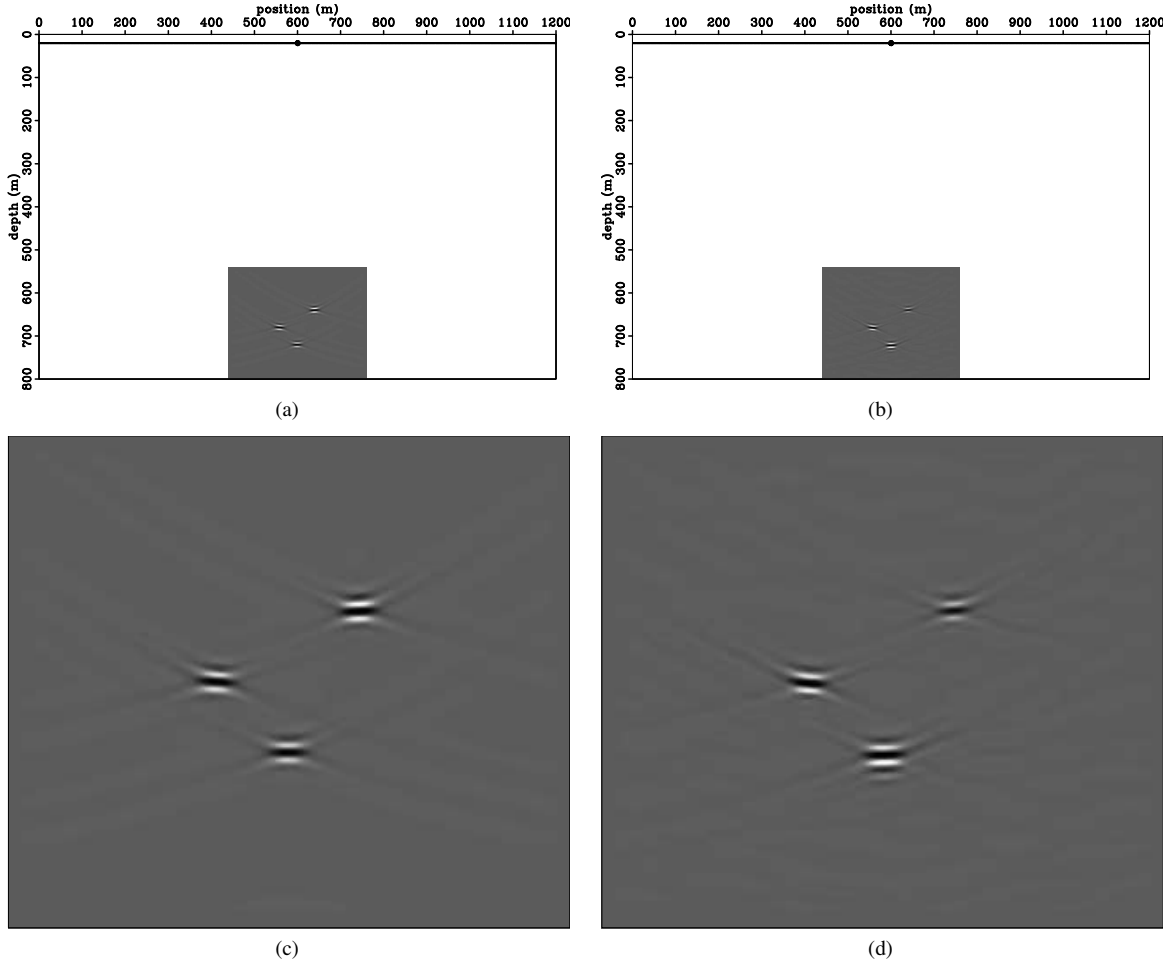


Figure 6. Images produced using the *interferometric imaging condition*. Panels (a) and (c) correspond to modeling and imaging with the smooth and known velocity model v_0, while panels (b) and (d) correspond to modeling using the random velocity model v and imaging using the smooth velocity model v_0. Panels (c) and (d) depict enlarged versions of the images shown in panels (a) and (b), respectively.

of the model is described by $\sigma = 0, 15, 30, 45\%$, respectively. As expected, the wavefronts recorded at the surface are increasingly distorted to the point where some of the later arrival are not even visible in the data.

Migration using conventional imaging condition leads to the images in figures 8(e)-8(h). As expected, the images show stronger artifacts due to the larger defocusing caused by the unknown random fluctuations in the model. However, migration using the interferometric imaging condition leads to the images in figures 8(i)-8(l). Artifacts are significantly reduced and the images are much better focused. While a complete theoretical study of the proposed functional remains to be done, the numerical results confirm its efficiency in complicated imaging regimes. This theoretical analysis falls outside the scope of this paper and remains subject for future investigation.

4 IMAGING EXAMPLES

There are many potential applications for this interferometric imaging functional. The application we concentrate on in this paper refers to imaging complex stratigraphy through a medium characterized by random variation. Accurate imaging in this situation requires velocity models that incorporate all random velocity variations. However, practical migration velocity analysis does not produce models of this level of accuracy, but approximates them with smooth, large-scale fluctuations one order of magnitude larger than that of the typical seismic wavelength. Here, we study the impact of the unknown (random) component of the velocity model on the images and whether interferometric imaging increases the image statistical stability.

For all our examples, we extrapolate wavefields using time-domain finite-differences both for modeling and for migration.

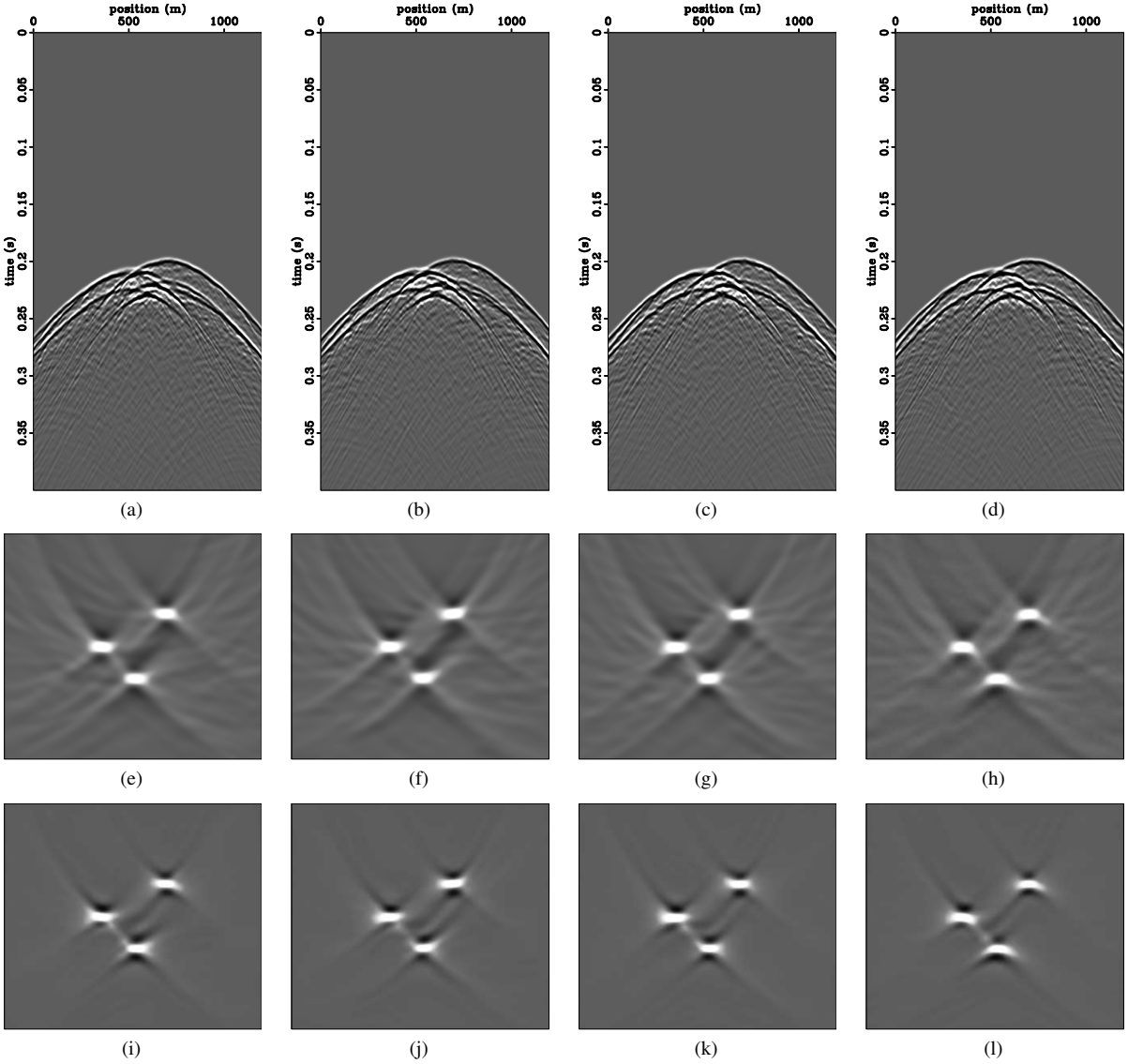


Figure 7. Illustration of statistical stability for the interferometric imaging condition in presence of random model variations. Data modeled with velocity with random variations with magnitude $\sigma = 20\%$, for different realizations of the noise model n. Images obtained by conventional imaging (e)-(h) and images obtained by interferometric imaging (i)-(l).

Thus, we simulate a reverse-time imaging procedure, although the theoretical results derived in this paper apply equally well to other wavefield reconstruction techniques, e.g. downward continuation, Kirchhoff integral methods, etc.

The parameters used in our examples, explained in Appendix A, are:

- seismic spatial wavelength $\lambda = 20$ m,
- wavelet central frequency $\omega = 150$ Hz,
- background velocity: $v_0 = 3000 + k\,z$ m/s ($k = 1s^{-1}$),
- random fluctuations parameters: $r_a = 30$, $r_c = 5$, $\alpha = 2$, and
- random velocity v constructed from the background velocity v_0.

Consider the model depicted in figures 10(a)-10(f). As in the preceding example, the left panels depict the known smooth velocity v_0, and the right panels depict the model with random variations. The imaging target is represented by the oblique lines, figure 9(b), located around $z = 700$ m, which simulate a cross-section of a complex stratigraphic model (e.g. meandering channels).

We model data with random velocity and image using the smooth model. Figures 10(a)-10(f) show wavefield snapshots in the two models for different propagation times, one before the source wavefields interact with the target reflectors and one after

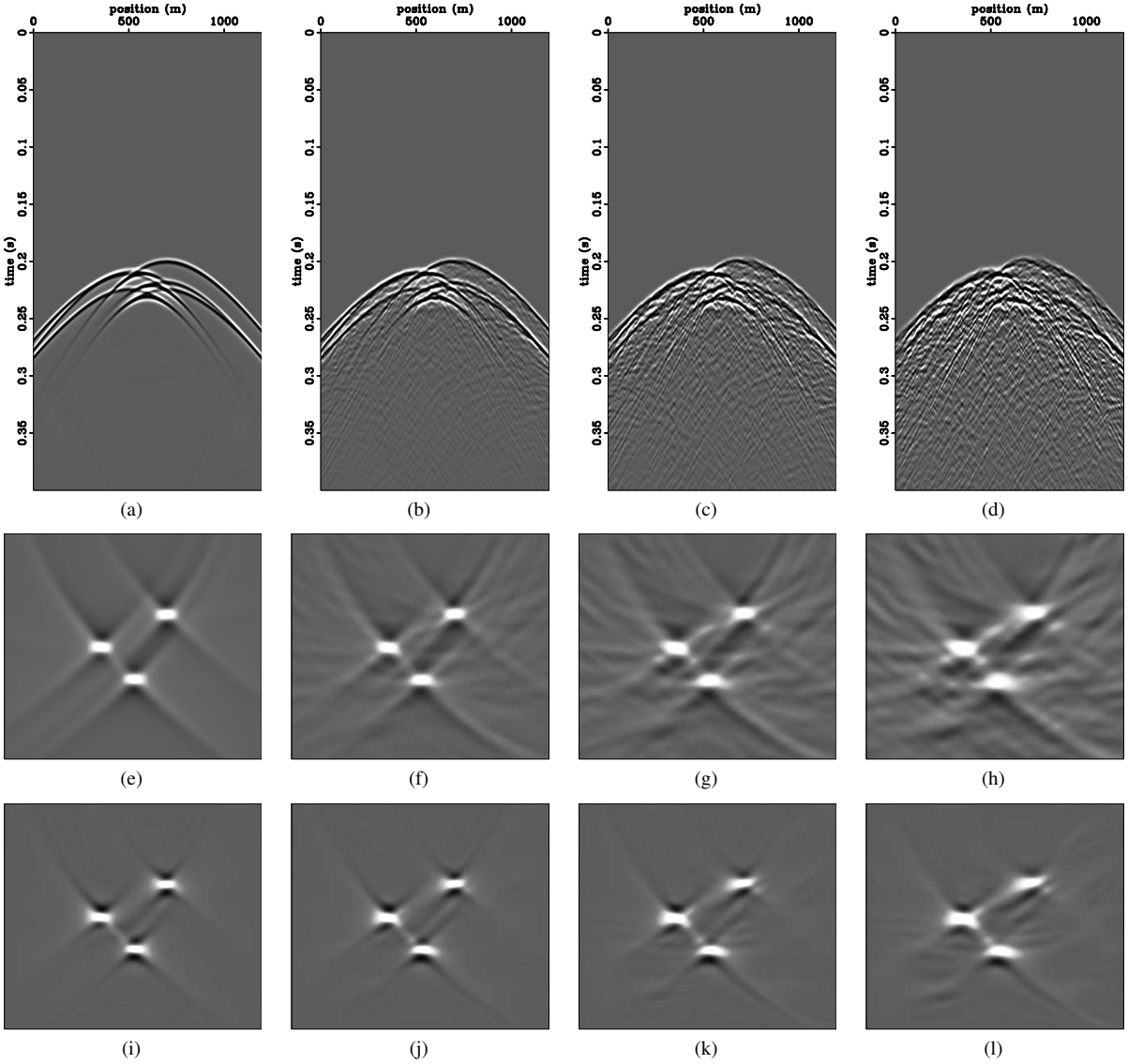
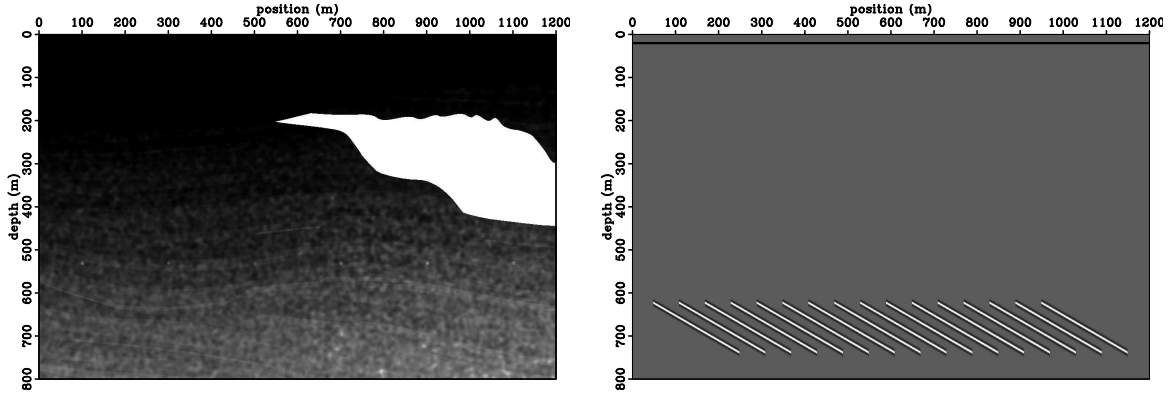


Figure 8. Illustration of interferometric imaging condition robustness in presence of random model variations. Data modeled with velocity with random variations with magnitude $\sigma = 0\%$ (a), $\sigma = 15\%$ (b), $\sigma = 30\%$ (c), and $\sigma = 45\%$ (d). Images obtained by conventional imaging (e)-(h) and images obtained by interferometric imaging (i)-(l).

this interaction. Figures 11(a) and 11(b) show the corresponding recorded data on the acquisition surface located at $z = \lambda$, where λ represents the wavelength of the source pulse.

Migration with conventional imaging condition of the data simulated in the smooth model using the smooth velocity produces the images in figures 12(a)-12(c). The targets are well imaged, although the image also shows artifacts due to truncation of the data on the acquisition surface. In contrast, migration with the conventional imaging condition of the data simulated in the random model using the smooth velocity produces the images in figures 12(b)-12(d). Those images are distorted by the random variations in the model that are not accounted for in the smooth migration velocity. The targets are hard to discern since they overlap with many truncation and defocusing artifacts caused by the inaccurate migration velocity. Finally, figures 13(a)-13(c) show the migrated images for the same situation as the one depicted in figures 12(a)-12(c), except that migration uses the interferometric imaging condition from equation (5). In this situation, since we are using the same model for modeling and migration, the interferometric imaging condition is not expected to change the image much. Interestingly, some of the truncation artifacts are attenuated, but otherwise the images are similar and the targets are easy to identify. Similarly, figures 13(b)-13(d) show the migrated images for the same situation as the one depicted in figures 12(b)-12(d), with migration using the interferometric imaging condition in



(a) (b)

Figure 9. Random velocity model (a) and imaging target located around $z = 700$ m (b).

equation (5). Many of the artifacts caused by the inaccurate velocity model are suppressed and the imaging targets are more clearly visible and easier to interpret. Furthermore, the general patterns of amplitude variation along the imaged reflectors are similar between figures 12(d) and 13(d). We note that the reflectors are not as well imaged as the ones obtained when the velocity is perfectly known. This is because the interferometric imaging condition described in this paper does not correct kinematic errors due to inaccurate velocity. It only acts on the extrapolated wavefields to reduce wavefield incoherency and add statistical stability to the imaging process. Further extensions to the interferometric imaging condition can improve focusing and enhance the images by correcting wavefields prior to imaging. However, this topic falls outside the scope of this paper and we do not elaborate on it further.

5 DISCUSSION

The interferometric imaging conditions defined by equations (5) or (7) represent extensions of conventional cross-correlation imaging conditions. Statistical stability in presence of model random variations is achieved by averaging in local windows in space and time. The computational cost of interferometric imaging condition is proportional to the number of samples in the image multiplied by the number of cross-correlation lags involved in the local space and time averaging, i.e. the size of the image times the sizes of the decoherence length and time. When the size of the decoherence windows is reduced to zero, the interferometric imaging condition becomes similar to the conventional autocorrelation imaging condition with identical properties and implementation cost.

As indicated earlier, the actual method used for wavefield reconstruction is not relevant for our discussion about this imaging condition. Any type of wavefield extrapolation can be substituted when reconstructing Green's functions in the velocity model without random variation. Thus, this form of imaging condition can be applied equally well to migration by downward continuation using space, wavenumber or mixed space-wavenumber extrapolation, reverse-time migration or Kirchhoff migration.

Areas of application for interferometric imaging include geologic areas with rapid velocity variations caused by stratigraphic features unaccounted for in typical velocity analysis or imaging through highly scattering media, e.g. basalt, anhydrite or inhomogeneous salt.

6 CONCLUSIONS

Conventional seismic imaging conditions based on wavefield cross-correlations are extended to achieve statistical stability for models with rapid, small-scale velocity variations. Random velocity variations on a scale comparable with the seismic wavelength are modeled by correlated Gaussian distributions.

Statistical stability is achieved by local averaging of cross-correlated wavefields at image locations. The proposed interferometric imaging condition is a natural extension of and reduces to the conventional cross-correlation imaging condition when the averaging window is made infinitely small.

The main characteristic of the method is that it operates on extrapolated wavefields at image positions (thus the name *interferometric imaging condition*), in contrast with alternative approaches involving migration of interferograms obtained by local data cross-correlations on the acquisition surface.

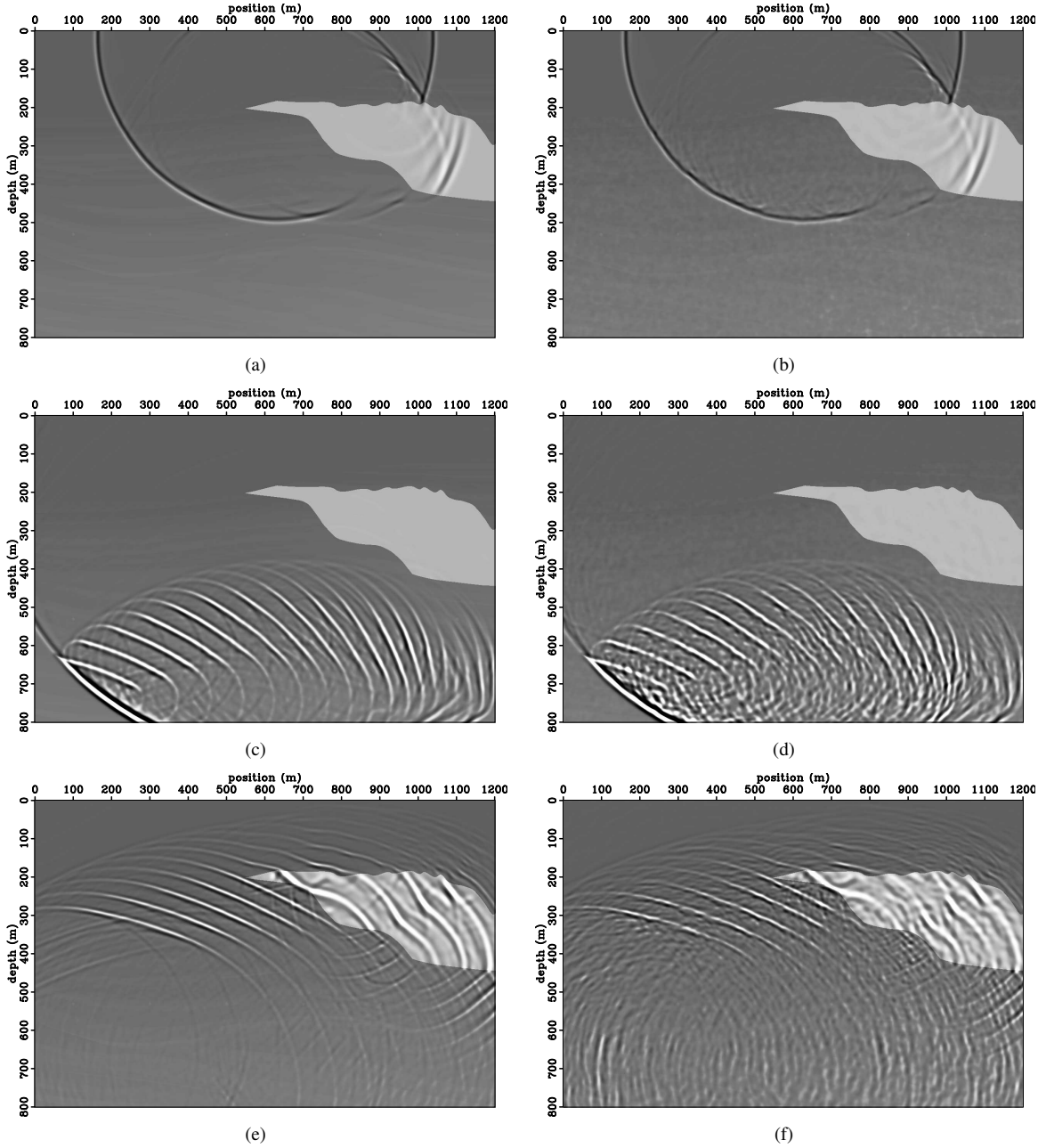


Figure 10. Wavefields simulated in the smooth background velocity v_0, panels (a) and (c) and in the random velocity v, panels (b) and (d).

REFERENCES

Artman, B., 2006, Imaging passive seismic data: Geophysics, **71**, SI117–SI187.

Artman, B., G. Alvarez, and K. Matson, 2007, Image-space surface-related multiple prediction: Geophysics, **72**, S113–S122.

Biondi, B. and W. W. Symes, 2004, Angle-domain common-image gathers for migration velocity analysis by wavefield-continuation imaging: Geophysics, **69**, 1283–1298.

Borcea, L., G. Papanicolaou, and C. Tsogka, 2005, Interferometric array imaging in clutter: Inverse Problems, **21**, 1419–1460.

———, 2006a, Adaptive interferometric imaging in clutter and optimal illumination: Inverse Problems, **22**, 1405–1436.

———, 2006b, Coherent interferometric imaging in clutter: Geopysics, **71**, SI165–SI175.

———, 2006c, Coherent interferometry in finely layered random media: SIAM Journal on Multiscale Modeling and Simulation, **5**, 62–83.

Claerbout, J. F., 1985, Imaging the Earth's interior: Blackwell Scientific Publications.

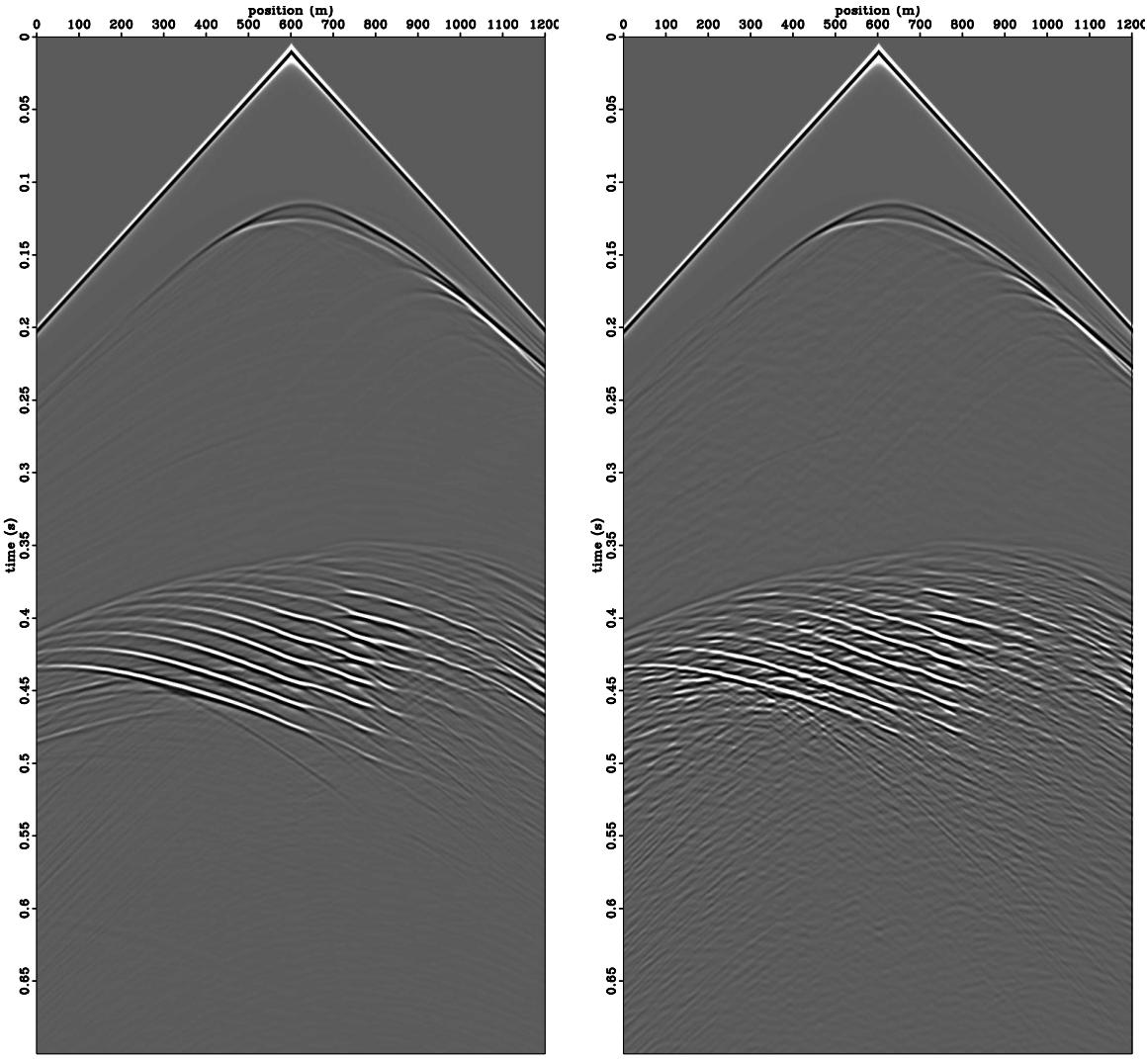


Figure 11. Data recorded for the smooth velocity model, panel (a), and for the model with random velocity variations, panel (b).

Dussaud, E., 2005, Velocity analysis in the presence of uncertainty: Ph.D. Thesis, Rice University.

Fink, M., 1999, Time-reversed acoustics: Scientific American, **281**, 91–97.

Fomel, S., 2004, Theory of 3-D angle gathers in wave-equation imaging, *in* 74th Ann. Internat. Mtg., Soc. of Expl. Geophys.

Fouque, J., J. Garnier, A. Nachbin, and K. Solna, 2005, Time reversal refocusing for point source in randomly layered media: Wave Motion, **42**, 191–288.

Kosloff, D. D. and E. Baysal, 1983, Migration with the full acoustic wave equation: Geophysics, **48**, 677–687.

Papanicolaou, G., L. Ryzhik, and K. Solna, 2004, Statistical stability in time reversal: SIAM J. Appl. Math., **64**, 1133–1155.

Pratt, R. G., 1990, Inverse theory applied to multi-source cross-hole tomography. part 2: Elastic wave-equation method: Geophys. Prosp., **38**, 311–312.

Pratt, R. G. and M. H. Worthington, 1990, Inverse theory applied to multi-source cross-hole tomography. part 1: Acoustic wave-equation method: Geophys. Prosp., **38**, 287–310.

Rickett, J. and P. Sava, 2002, Offset and angle-domain common image-point gathers for shot-profile migration: Geophysics, **67**, 883–889.

Sava, P. and B. Biondi, 2004a, Wave-equation migration velocity analysis - I: Theory: Geophysical Prospecting, **52**, 593–606.

———, 2004b, Wave-equation migration velocity analysis - II: Subsalt imaging examples: Geophysical Prospecting, **52**, 607–623.

Sava, P. and S. Fomel, 2003, Angle-domain common image gathers by wavefield continuation methods: Geophysics, **68**, 1065–1074.

———, 2005, Coordinate-independent angle-gathers for wave equation migration: 75th Ann. Internat. Mtg., Expanded Abstracts, 2052–2055, Soc. of Expl. Geophys.

———, 2006, Time-shift imaging condition in seismic migration: Geophysics, **71**, S209–S217.

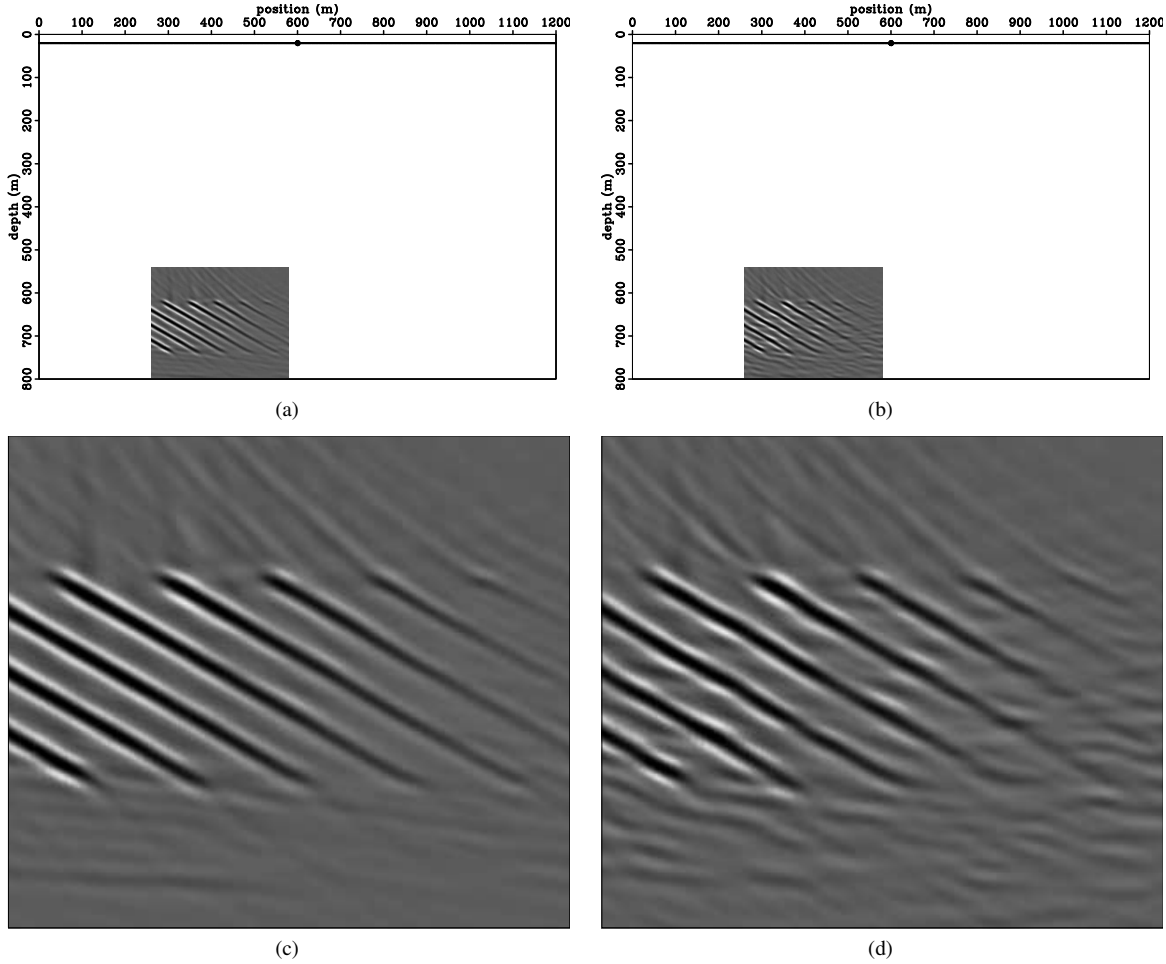


Figure 12. Images produced using the *conventional imaging condition*. Panels (a) and (c) correspond to modeling and imaging in the smooth known velocity model v_0, and panels (b) and (d) correspond to modeling using the random velocity model v and imaging using the smooth velocity model v_0. Panels (c) and (d) depict enlarged versions of the images shown in panels (a) and (b), respectively.

Shen, P., W. W. Symes, S. Morton, and H. Calandra, 2005, Differential semblance velocity analysis via shot profile migration: 2249–2253.
Stolk, C. C. and W. W. Symes, 2004, Kinematic artifacts in prestack depth migration: Geophysics, **69**, 562–575.
Tarantola, A., 1987, Inverse Problem Theory: methods for data fitting and model parameter estimation: Elsevier.
Woodward, M. J., 1992, Wave-equation tomography: Geophysics, **57**, 15–26.

7 APPENDIX A

7.1 Noise model

Consider a medium whose behavior is completely defined by the acoustic velocity, i.e. assume that the density $\rho(x,y,z) = \rho_0$ is constant and the velocity $v(x,y,z)$ fluctuates around a homogenized value $v_0(x,y,z)$ according to the relation

$$\frac{1}{v^2(x,y,z)} = \frac{1+\sigma m(x,y,z)}{v_0^2(x,y,z)}\,, \tag{A-1}$$

where the parameter m characterizes the type of random fluctuations present in the velocity model, and σ denotes their strength.

Consider the covariance orientation vectors

$$\mathbf{a} = \left(a_x, a_y, a_z\right)^\top \in \mathbb{R}^3 \tag{A-2}$$

$$\mathbf{b} = \left(b_x, b_y, b_z\right)^\top \in \mathbb{R}^3 \tag{A-3}$$

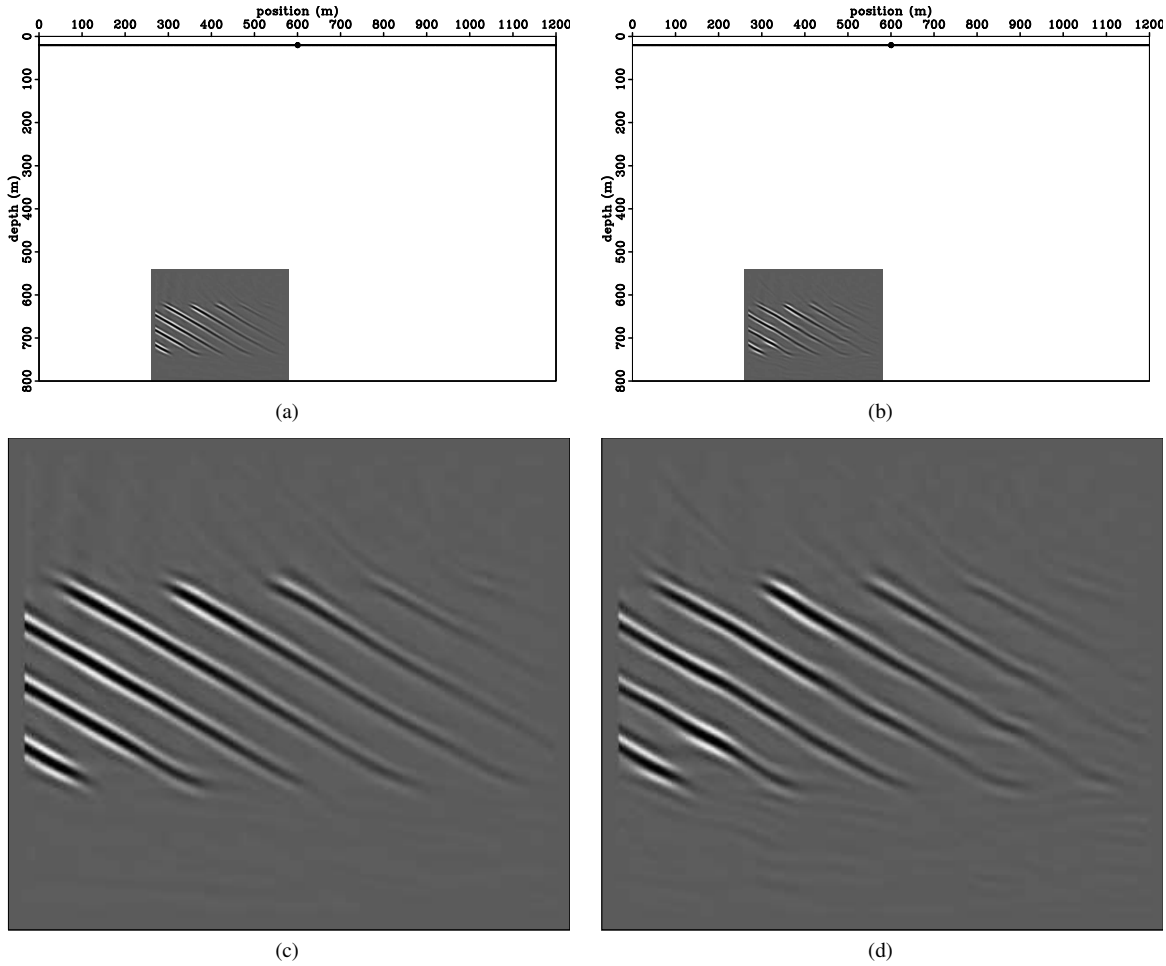


Figure 13. Images produced using the *interferometric imaging condition*. Panels (a) and (c) correspond to modeling and imaging with the smooth and known velocity model v_0, while panels (b) and (d) correspond to modeling using the random velocity model v and imaging using the smooth velocity model v_0. Panels (c) and (d) depict enlarged versions of the images shown in panels (a) and (b), respectively.

$$\mathbf{c} \quad = \quad \left(c_x, c_y, c_z\right)^\top \in \mathbb{R}^3 \tag{A-4}$$

defining a coordinate system of arbitrary orientation in space. Let $r_a, r_b, r_c > 0$ be the covariance range parameters in the directions of **a**,**b** and **c**, respectively.

We define a covariance function

$$\mathrm{cov}\left(x,y,z\right) = \exp\left[-l^{\alpha}\left(x,y,z\right)\right] , \tag{A-5}$$

where $\alpha \in [0,2]$ is a distribution shape parameter and

$$l\left(x,y,z\right) = \sqrt{\left(\frac{\mathbf{a}\cdot\mathbf{r}}{r_a}\right)^2 + \left(\frac{\mathbf{b}\cdot\mathbf{r}}{r_b}\right)^2 + \left(\frac{\mathbf{c}\cdot\mathbf{r}}{r_c}\right)^2} \tag{A-6}$$

is the distance from a point at coordinates $\mathbf{r} = (x,y,z)$ to the origin in the coordinate system defined by $\{r_a\mathbf{a}, r_b\mathbf{b}, r_c\mathbf{c}\}$.

Given the IID Gaussian noise field $n\left(x,y,z\right)$, we obtain the random noise $m\left(x,y,z\right)$ according to the relation

$$m\left(x,y,z\right) = \mathscr{F}^{-1}\left[\sqrt{\widehat{\mathrm{cov}}\left(k_x,k_y,k_z\right)}\,\widehat{n}\left(k_x,k_y,k_z\right)\right] , \tag{A-7}$$

where k_x, k_y, k_z are wavenumbers associated with the spatial coordinates x, y, z, respectively. Here,

$$\widehat{\mathrm{cov}} \quad = \quad \mathscr{F}\left[\mathrm{cov}\right] \tag{A-8}$$

$$\widehat{n} \quad = \quad \mathscr{F}\left[n\right] \tag{A-9}$$

are Fourier transforms of the covariance function cov and the noise n, $\mathscr{F}[\cdot]$ denotes Fourier transform, and $\mathscr{F}^{-1}[\cdot]$ denotes inverse Fourier transform. The parameter α controls the visual pattern of the field, and $\mathbf{a},\mathbf{b},\mathbf{c},r_a,r_b,r_c$ control the size and orientation of a typical random inhomogeneity.

7.2 Wave propagation and scale regimes

Acoustic waves characterized by pressure $p(x,y,z,t)$ propagate according to the second order acoustic wave-equation for constant density

$$\frac{\partial^2 p}{\partial t^2} = v^2\nabla^2 p + F_\lambda(t)\;, \tag{A-10}$$

where $F_\lambda(t)$ is a wavelet of characteristic wavelength λ.

Given the parameters l (size of inhomogeneities), λ (wavelength size), L (propagation distance) and σ (noise strength), we can define several propagation regimes:

- The *weak fluctuations regime* characterized by waves with wavelength of size comparable to that of typical inhomogeneities propagating over a medium with small fluctuations to a distance of many wavelengths. This regime is characterized by negligible back scattering, and the randomness impacts the propagating waves through forward multipathing. The relevant length parameters are related by

$$l \sim \lambda \ll L\;, \tag{A-11}$$

and the noise strength is assumed small

$$\sigma \ll 1\;. \tag{A-12}$$

- The *diffusion approximation regime* characterized by waves with wavelength much larger than that of typical inhomogeneities propagate over a medium with strong fluctuations to a distance of many wavelengths. This regime is characterized by traveling waves that are statistically stable but diffuse with time. Back propagation of such waves in a medium without random fluctuations results in loss of resolution. The relevant length parameters are related by

$$l \ll \lambda \ll L\;, \tag{A-13}$$

and the noise strength is not assumed small

$$\sigma \sim 1\;. \tag{A-14}$$

8 APPENDIX B

8.1 Time-domain implementation

The imaging functional (5) can be implemented in the frequency-domain or in the time-domain. However, the time-domain implementation is not an exact equivalent of the frequency-domain implementation, but an analog implementation, as explained in this appendix.

Consider the imaging functional (5) and restrict the analysis to the space variables $\mathbf{y}_h$:

$$\begin{aligned} I(\mathbf{y}_m) \quad = \quad & \int_{\omega_m} d\omega_m \int_{|\mathbf{y}_h|\le Y/2} d\mathbf{y}_h \\ & \overline{G_0(\mathbf{x}_s,\mathbf{y}_m-\mathbf{y}_h,\omega_m)} \int_{\mathbf{x}_m} d\mathbf{x}_m\, P(\mathbf{x}_m,\omega_m)\, \overline{G_0(\mathbf{x}_m,\mathbf{y}_m-\mathbf{y}_h,\omega_m)} \\ & \overline{\overline{G_0(\mathbf{x}_s,\mathbf{y}_m-\mathbf{y}_h,\omega_m)} \int_{\mathbf{x}_m} d\mathbf{x}_m\, P(\mathbf{x}_m,\omega_m)\, \overline{G_0(\mathbf{x}_m,\mathbf{y}_m+\mathbf{y}_h,\omega_m)}}\;. \end{aligned} \tag{B-1}$$

Expression (B-1) can be written equivalently as:

$$I(\mathbf{y}_m) = \int_{\omega_m} d\omega_m \int_{|\mathbf{y}_h|\le Y/2} d\mathbf{y}_h\, \overline{U_S(\mathbf{y}_m-\mathbf{y}_h,\omega_m)} U_R(\mathbf{y}_m-\mathbf{y}_h,\omega_m)\, \overline{\overline{U_S(\mathbf{y}_m+\mathbf{y}_h,\omega_m)} U_R(\mathbf{y}_m+\mathbf{y}_h,\omega_m)}\;, \tag{B-2}$$

where $U_S(,)$ represents the source wavefield and $U_R(,)$ represents the receiver wavefield reconstructed at various image locations, $\mathbf{y}_m-\mathbf{y}_h$ or $\mathbf{y}_m+\mathbf{y}_h$.

If we introduce the notation $U(,) = U_S(,)\ U_R(,)$, then we can write equation (B-2) as

$$I(\mathbf{y}_m) = \int\limits_{\omega_m} d\omega_m \int\limits_{|\mathbf{y}_h|\le Y/2} d\mathbf{y}_h\, U(\mathbf{y}_m - \mathbf{y}_h, \omega_m)\, \overline{U(\mathbf{y}_m + \mathbf{y}_h, \omega_m)}\,, \tag{B-3}$$

where the overline denotes cross-correlation of the wavefields $U(,)$ at coordinates $\mathbf{y}_m - \mathbf{y}_h$ and $\mathbf{y}_m + \mathbf{y}_h$.

The average cross-correlation of $U(\mathbf{y}_m - \mathbf{y}_h, \omega_m)$ and $U(\mathbf{y}_m + \mathbf{y}_h, \omega_m)$ can be written in the time domain as

$$I(\mathbf{y}_m, \tau) = \int\limits_{t} dt \int\limits_{|\mathbf{y}_h|\le Y/2} d\mathbf{y}_h\, U(\mathbf{y}_m - \mathbf{y}_h, t-\tau)\, U(\mathbf{y}_m + \mathbf{y}_h, t+\tau)\ , \tag{B-4}$$

therefore, the zero cross-correlation time lag imaging condition in the time domain can be written as

$$I(\mathbf{y}_m) = \int\limits_{t} dt \int\limits_{|\mathbf{y}_h|\le Y/2} d\mathbf{y}_h\, U(\mathbf{y}_m - \mathbf{y}_h, t)\, U(\mathbf{y}_m + \mathbf{y}_h, t)\ . \tag{B-5}$$

We can also achieve higher stability by local time averaging in windows of size T:

$$I(\mathbf{y}_m) = \int\limits_{t} dt \int\limits_{|\tau|\le T/2} d\tau \int\limits_{|\mathbf{y}_h|\le Y/2} d\mathbf{y}_h\, U(\mathbf{y}_m - \mathbf{y}_h, t-\tau)\, U(\mathbf{y}_m + \mathbf{y}_h, t+\tau)\ . \tag{B-6}$$

Expression equation (**??**) represents an imaging functional for seismic data, since if the windows Y and T reduce to one sample in space and time, the image is formed by the auto-correlation of the extrapolated wavefields. If the the zero-lag of the cross-correlation of the source and receiver wavefields maximizes at an image point, the auto-correlation of this function also maximizes at the same location.